

Virtual simulation of the postsurgical cosmetic outcome in patients with *Pectus Excavatum*

João L. Vilaça^{*a,b}, António H. J. Moreira^a, Pedro L-Rodrigues^a, Nuno Rodrigues^{b,c}, Jaime C. Fonseca^d, A.C.M. Pinho^e, Jorge Correia-Pinto^a

^aLife and Health Sciences Research Institute, University of Minho. 4710-057 Braga, Portugal;

^bDIGARC – Polytechnic Institute of Cávado and Ave 4750-810 Barcelos, Portugal;

^cDI-CCTC University of Minho 4710-057 Braga;

^dIndustrial Electronics Department, University of Minho, 4710-057, Portugal;

^eMechanical Department, University of Minho, 4710-057 Guimarães, Portugal

ABSTRACT

Pectus excavatum is the most common congenital deformity of the anterior chest wall, in which several ribs and the sternum grow abnormally. Nowadays, the surgical correction is carried out in children and adults through Nuss technic. This technic has been shown to be safe with major drivers as cosmesis and the prevention of psychological problems and social stress. Nowadays, no application is known to predict the cosmetic outcome of the *pectus excavatum* surgical correction. Such tool could be used to help the surgeon and the patient in the moment of deciding the need for surgery correction. This work is a first step to predict postsurgical outcome in *pectus excavatum* surgery correction. Facing this goal, it was firstly determined a point cloud of the skin surface along the thoracic wall using Computed Tomography (before surgical correction) and the Polhemus FastSCAN (after the surgical correction). Then, a surface mesh was reconstructed from the two point clouds using a Radial Basis Function algorithm for further affine registration between the meshes. After registration, one studied the surgical correction influence area (SCIA) of the thoracic wall. This SCIA was used to train, test and validate artificial neural networks in order to predict the surgical outcome of *pectus excavatum* correction and to determine the degree of convergence of SCIA in different patients. Often, ANN did not converge to a satisfactory solution (each patient had its own deformity characteristics), thus invalidating the creation of a mathematical model capable of estimating, with satisfactory results, the postsurgical outcome.

Keywords: *Pectus Excavatum*, 3D simulation, image processing, affine registration between meshes, artificial neural network

1. INTRODUCTION

Pectus excavatum is the most common congenital deformity of the thoracic wall, which demands surgical correction in a high percentage of cases. This deformity involves the sternum and the cartilages, being detected in the childhood and happening in 1:1000 births with male predominance of 4 to 1 [1, 2]. The *pectus excavatum* can present moderate concave depressions that range from a few millimeters to severe asymmetrical depressions with wide centimeters (Fig. 1).

Since the initial report of minimal invasive repair of *pectus excavatum*, described by Donald Nuss in 1998, it has gained world-wide acceptance and popularity for the repair of *pectus excavatum* in children and adults [3].

This technique has been shown to be safe with good cosmetic results. The surgical procedure involved, utilizes two symmetric incisions in the lateral thoracic wall, through which a convex prosthesis is placed into the substernal position to leverage the deformity into a more anatomically correct position [4]. To prevent prosthesis displacements during chest wall reshape, a stabilizer bar is coupled at each end. A non-absorbable suture or wire is finally placed around the ribs, so that the prosthesis and the bar stabilizer to secure them as a single unit [5]. The surgical prosthesis is left in place for 24 to 36 months, after which it is removed by reopening the lateral incision.

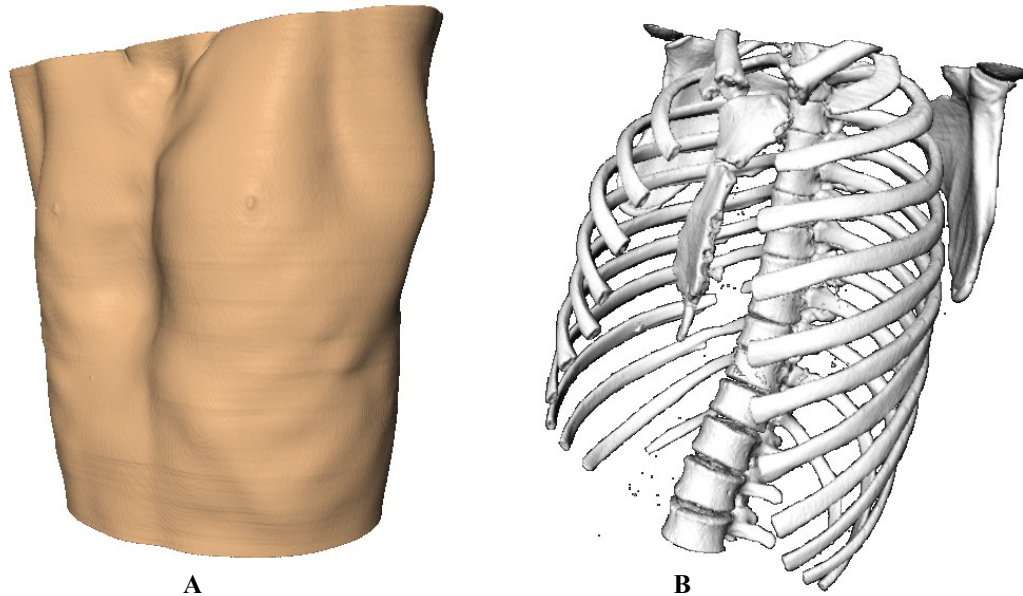


Figure 1. 3D reconstruction images acquired with Computed Tomography scan. A - The image-reconstruction with soft tissues in which it is perceived the defects of the chest wall (*pectus excavatum*). B - Image reconstruction of the bones chest wall where the abnormal positioning of the sternum is identified.

The surgical correction of this deformity is usually executed for the cosmetic improvement and prevention of psychological problems in the patient, not being usually associated to sufficiently serious cardio-pulmonary dysfunctions that may affect the normal life of the patient. However, some patients with moderate or serious *pectus excavatum* severity can present moderate displacement of the lungs and heart, causing lack of resistance and consequently some intolerance to physical exercises [6, 7]. Many times, the associated psychological problems leave social isolation and loss of self-confidence, especially in adolescence.

Given the clinical context surrounding *pectus excavatum*, the existence of a graphical software for postoperative result simulation of the *pectus excavatum* surgical correction (PESC) is of utmost importance. Among other applications, such a tool would help both surgeon and patient to access the need for the surgery as well as to understand how such a procedure would improve the patient's physical aspect.

The development of such a tool mostly depends on the knowledge about how the patient's thoracic wall surface change with PESC. This work presents an evaluation of the thoracic wall surface modifications after PESC in 21 patients and analyses, for those patients, the degree of convergence of the thoracic wall surface. The outcome of this analysis allows the definition of a surgical correction influence area (SCIA), which could be used to simulate and predict the *pectus excavatum* postoperative result.

The remainder of the paper is organized as follows. Section II describes related work and the main contributions of this our work, section III presents an overview of the developed and used methods, section IV outlines statistical results, and section V presents some conclusions and future work.

2. RELATED WORK

To the best of the authors knowledge, there are no applications capable of predict the cosmetic outcome of the surgical correction of *pectus excavatum*. In this work one analyses the possibility of the development of a software tool, based on artificial neural networks (ANN), to predict the surgical result.

ANN are mathematical models with biological inspirations based on various characteristics of the brain functionality. They are highly parallel connectionist systems composed of many simple elements (artificial neurons). A single ANN is composed of three layers (input layer, hidden layer and output layer) interconnected with different weights that propagate signals through the network [8].

In the last decade, ANN has been a valuable tool in the medicine field, especially due to their ability to approximate nonlinear functions, pattern recognition and association. The published literature suggests that ANN models have been shown to be valuable tools in reducing the workload of clinicians, by detecting and providing decision support systems of medical applications [9].

Archambeau *et al.* used ANN for predicting the features of visual sensations in order to develop an optic nerve to restore partial vision. ANN were able to decode and model the physiological process linking the stimulating parameters to the visual sensations produced in the visual field of a blind volunteer [10]. [11] presents a computer-based decision support system for automated interpretation of diagnostic heart images. The system was based on image processing techniques, ANN and large well-validated medical databases.

Recent advances in the field of ANN have made them attractive for analyzing signals. Some of these applications in the medical domain include Doppler signals [12], diagnosis of myocardial infarction [13], electrocardiogram analysis [14] and image processing of medical images [15].

Generally, the determination of the ANN architecture is a complex problem and cannot be easily solved. There are four elements that comprise the ANN architecture definition: number of layers; number of neurons in each layer; activation function of each layer; and, training algorithm that determines the final value of the weights and biases [16, 17].

Many authors discuss the question of approximation by feed-forward neural networks (FNN) and cascade-forward networks (CNN). CNN are similar to FNN, but include a weight connection from the input to each layer and from each layer to the successive layers. This new connection might improve the learning process of the network [17-19]. The first main advantage is that these networks learn from non-linear relationships, not requiring a user-specified problem solving algorithm. Moreover, they also present inherent generalization ability, since they can identify and respond to patterns that are similar but not identical to the ones with which they have been trained. FNN and CNN can potentially represent any input-output relationship with a finite number of discontinuities, assuming that there are enough neurons in the hidden layer. The main disadvantage is that there is no prior guarantee that the model will perform well and converge to one acceptable solution for the problem at hand. In many studies these topologies are trained using a backpropagation algorithm, based on gradient descent techniques to update the weights and biases of the network in accordance to a performance function.

Based on ANN research, this work tests an improved solution to predict the outcome of *pectus excavatum* surgical correction based on FNN and CNN. Due to their ability to approximate non-linear relationships, several FNN and CNN were developed based on different training algorithms that use skin surface information gathered before and after the PESC. The following steps were taken in order to determine the data sets of the FNN and CNN training procedure:

- i) Acquirement of the skin points of the thoracic wall in patients with *pectus excavatum* before surgery using Computed Tomography (CT) images and image processing techniques;
- ii) Assessment of the skin points along the thoracic wall after surgical correction of the same patients, using a 3D scanner without any radiation [20];
- iii) Merging of unorganized point clouds for 3D surface reconstruction of points acquired from the 3D scanner and CT images, followed by Laplacian smoothing;
- iv) 3D affine registration between the two resulting meshes of the previous step;

- v) Measurement of the *pectus excavatum* deformity differences before and after surgical correction, based on distances between two triangular meshes resulting from the affine registration. This study will make possible to define the maximal area of the thoracic wall that suffers deformation after the surgical correction;
- vi) Training of FNN and CNN based on the distance samples from the previous step, to simulate and predict the *pectus excavatum* postoperative result.

3. METHODS

The following section describes different developed modules and their structural workflow to obtain the FNN and CNN training vectors: skin points of the thoracic wall before and after PESC (Fig. 2).

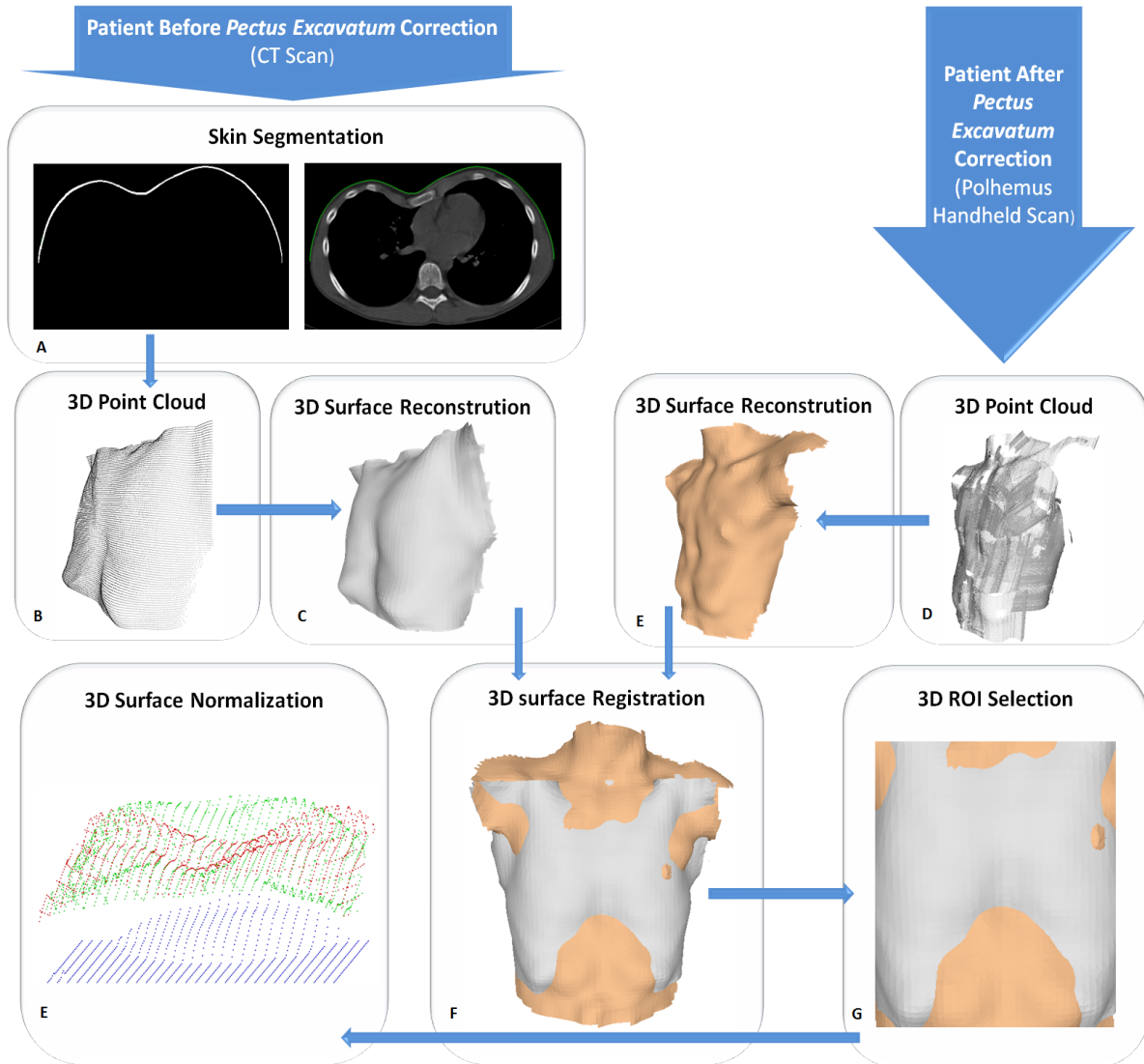


Figure 2. Overview of the processing results between the different developed modules to determine FNN and CNN training vectors.

The information of the patient thoracic wall was acquired using two different scanning techniques (CT scan and a 3D scanner) captured in two different moments (before and after PESC), which resulted in different data sets. For training the FNN and CNN, the training vectors must have the same point's density and represent the same thoracic region before and after the surgery for all patients. This led to a correspondence problem between the two data sets (Fig. 2F). In order to overcome this problem, the two data sets were previously processed and reconstructed in continuous surfaces of the skin (Fig. 2 B, C, D and E). After establishing the correspondence between the two data sets, one defined a volume of interest (VOI) (Fig. 2G) based on SCIA, in order to normalize each data set (Fig. 2E).

The following subsections describe in detail the different developed modules.

3.1. Assessment point cloud along the anterior chest wall

3.1.1. Before surgery correction

CT scans remain the primary modality for preoperative imaging of *pectus excavatum*, providing useful information on abnormal thoracic anatomy and symmetry defects. Since a CT examination is always carried out before surgery, all points belonging to the skin surface along the thoracic wall, were acquired in CT images resorting to image processing techniques.

Considering that most noise corrupted CT images have a Gaussian distribution, a Gaussian filter was implemented. This initial step was essential to obtain the meaningful image information and reduce image noise level [21]. The standard deviation of the Gaussian filter was experimentally calculated with a final result of $\sigma = 2.5$ pixels. Subsequently, all CT images showed up with a black background colour, facilitating the segmentation of the skin surface contour by a Sobel operator. Then, all image pixels, from all slices of the 3D CT data set, were vertically and horizontally tracked by recursively selecting all first pixels belonging to image gradient magnitude and taking into account the coronal plane (assumed as the one calculated by the vertical component value of the rightist and leftist ribs points). The result of this procedure was the skin substructure illustrated in Fig. 2A (green and white points).

3.1.2. After surgery correction

Although CT scan has been a compulsory examination to assess *pectus excavatum* severity before surgery, this image examination was not used after surgery, because CT scan submits the patient to larger amounts of radiation when compared to other imaging modalities. In order to avoid another CT scan, the assessment of anterior chest wall points, after PESC was done using the Polhemus FastSCAN, without involving any radiation to the patient.

Polhemus FastSCAN system is a portable 3D scanner capable of creating instant real time 3D images. This system integrates a track unit to determine the position and orientation of a laser line on the object while a camera detects the laser to record cross-sectional depth profiles. By combining these two characteristics, motion tracking and laser recording, this system enables the computer to reconstruct a full 3D surface. The most important characteristics of the employed system are the following:

- Laser resolution typically 0.5mm, as good as 0.1mm;
- Laser scanning rate up to 50 lines/second;
- Scanning range up to 750mm;
- Absolute accuracy of 0.75mm.

In order to achieve a minimal error during acquisition, due to patient and respiratory movements, the system reference was attached to the 10° left rib of the rib cage. The best laser scanning paths were achieved from the top to the bottom of the thoracic wall. Scanning paths taken from the left to the right side of the thoracic wall show higher scan misalignment on the right side of the patient, due to the increased distance to the reference.

3.2. Surface reconstruction

Surface reconstruction from cloud points is an essential tool in computer graphics, being widely studied and a well-known problem. On the last decades several methods have appeared, whether for structured or unstructured cloud-points [22-26].

In this work, most of the point clouds acquired from the 3D scanner appeared as unorganized sample data, with useless information and outliers, containing noise and non-uniformities in thickness and spacing. Some of these errors are related to body and respiratory movements or misalignment of the scan reference. As shown in Fig 3 A, C, and E the gray level distributions are related to the number of points acquired from the 3D scanner: darker gray levels have more points than the lighter gray levels in Oy plane.

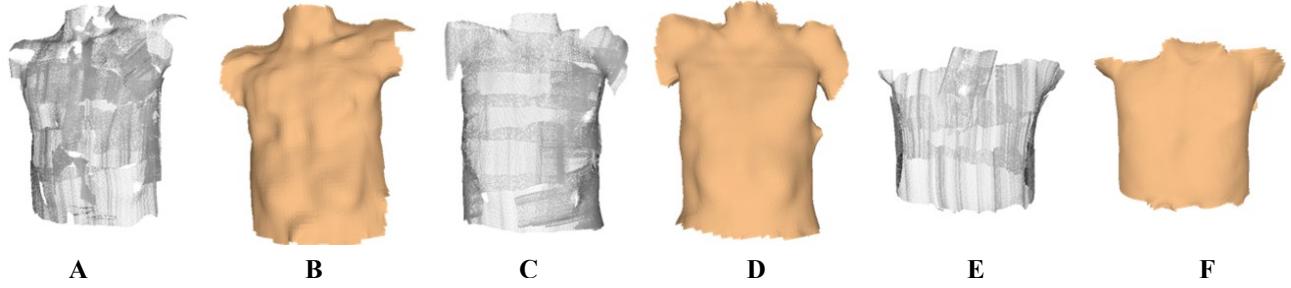


Figure 3. Mesh repair and reconstruction using Radial Basis Functions (RBF) of skin surface samples from 3D scanner.

During surface reconstruction it was necessary to ensure smooth blending between different point clouds in different Oy planes (darker gray levels Fig 3 A, C and E), re-meshing of existing noisy, good consolidation, redistribution of the input points and the ability to fill holes.

The algorithm used to reconstruct a smooth surface from the raw points of CT images and the 3D scanner was based on Radial Basis Functions (RBFs), firstly introduced by Savchenko *et al.* [27]. In general, RBF is a function of form (Eq. 1):

$$s(x) = p(x) + \sum_{i=1}^N \lambda_i \phi(x - x_i) \quad (1)$$

where p is a polynomial of low degree and the basic function ϕ is a real valued function on $[0; \infty]$, usually unbounded and of non-compact support. λ_i and x_i are weights and centers of the RBF, respectively [28].

Some well-known benefits of modeling surfaces with RBFs improved the output mesh quality from the data acquired with the 3D scanner and CT imagiology (Fig. 3 B, D and F) [22, 27, 29].

However, in some cases, the RBF algorithm produced a mesh with excessive smoothness, losing some fundamental characteristics, with to the 3D affine registration in the next section. In these cases some parameters from the RBF algorithm computation were changed, mainly to increase fit accuracy and mesh resolution:

- The voxel size of the reconstruction - this way when two or more samples overlap in the same Oy plane, their contribution blend smoothly, hiding possible misalignments;
- Widening - used to fill holes between sample points and re-meshing.

Then, it was used a Laplacian smoothing to clean out eventually noisy borders.

In the end of this subsection, two 3D meshes were created: one representing the anterior thoracic wall before PESC (constructed using a point cloud determined in subsection 3.1.1) and another representing the anterior thoracic wall after PESC (constructed using a point cloud determined in subsection 3.1.2).

3.3. Surface affine registration

Affine surface registration consists on the estimation and matching of corresponding regions (references) in two different 3D meshes, in order to determine the translations and/or rotations in $Oxyz$ that best align each other.

Given the two meshes calculated on the previous section (Fig. 4A) in arbitrary initial poses, matching pairs of points (Fig. 4B) generates a set of candidate transformations between them. The best alignment was achieved by getting the points from one mesh to the closest distance of the other.

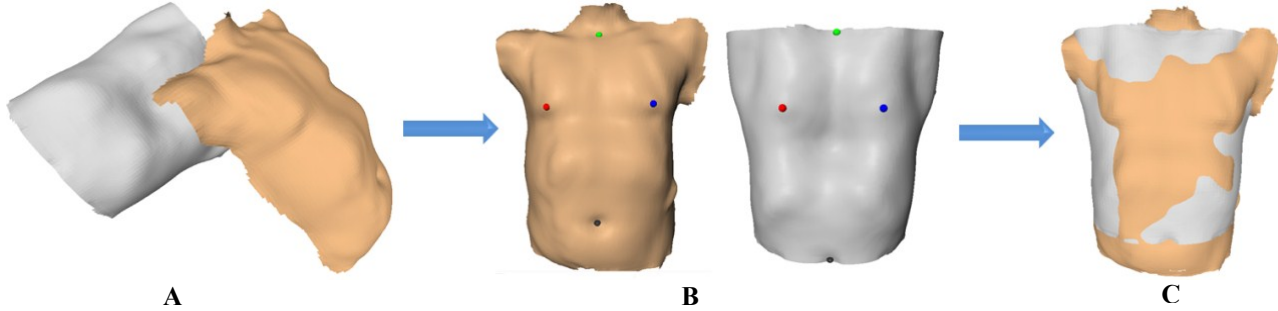


Figure 4. Four pairs of points used to surface registration: anterior thoracic wall before PESC in gray level and anterior thoracic wall after PESC in skin colour.

This work presents an algorithm, based on [30], to semi-automatically register these two meshes, commonly with rather small overlap (Fig. 4A). The method makes assumption of four pairs of corresponding vectors, Xi and Xf , in each mesh (Fig. 4B).

Mathematically, one vector Xi can be transformed in another vector Xf by multiplying one of them by a matrix M as follows (Eq. 2):

$$\begin{bmatrix} x_{fn} \\ y_{fn} \\ z_{fn} \end{bmatrix} = \begin{bmatrix} m00 & m01 & m02 \\ m10 & m11 & m12 \\ m20 & m21 & m22 \end{bmatrix} \begin{bmatrix} x_{in} \\ y_{in} \\ z_{in} \end{bmatrix} \quad (2)$$

The matrix transformation M was calculated based on four pairs of vectors Xi and Xf , respectively, and by solving a 12 equations system. Then, scaling factors $\alpha_x, \alpha_y, \alpha_z$ along Ox, Oy and Oz axis, respectively, were determined for each pair of points. The scaling transformation was achieved by multiplying $m00, m11$ and $m22$ of the M matrix by the average of all factors α_x, α_y and α_z in each direction. This matrix can represent any affine transformation, including scaling, rotation and translation.

The four pairs of points were chosen as follows (Fig. 4B): one on the neck, one on navel and one on each breast nipple. Sometimes, the breast nipples were not clear due to the Laplacian smooth needed in the surface reconstruction. In these cases, one has chosen the higher points of the low ribs of the thoracic wall.

3.4. VOI Selection

The *pectus excavatum* deformity can present moderate concave depressions with few millimeters to severe asymmetrical depressions with wide centimeters. Through the surgical correction of *pectus excavatum*, a huge region of the anterior chest wall is reshaped, with 3D transformations above, bellow, on the left and on the right sides of the deformity largest depression point. So far, no study presents how these transformations occur along the anterior chest wall and whether they manifest themselves equally from patient to patient.

This sub section presents a comparative analysis between the anterior chest wall surface acquired before and after the PESC. It aims at the definition of the patients SCIA for establishing the anterior chest wall VOI. Different parameters were defined and analyzed to characterize SCIA, most of them related to the deformity largest depression point, as follows (Fig. 5C): upper distances, lower distance (in this measure it was defined an end limit that corresponds to the end of ribs cage), left and right sides. The maximum value of each measure was used to define the VOI between the two meshes obtained in subsection 3.3.

As shown in Fig. 5A and B, the mean values of upper and lower distances, as well the distances on the right and left side, are similar. This means that PESC usually occurs similarly in all directions of the anterior chest wall, starting at the point of greatest depression. However, some diverging measures and outliers were also found. This demonstrates the idiosyncrasy of each patient and could indicate the difficulty in finding similar characteristics between them, especially in asymmetric patients.

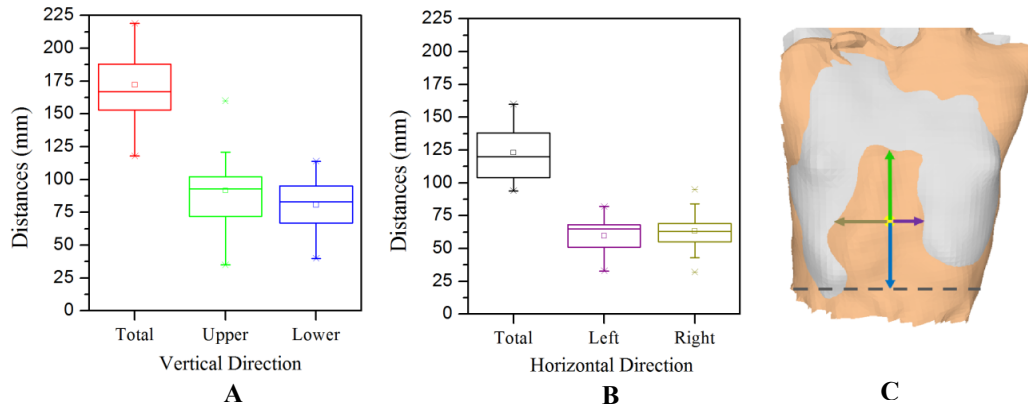


Figure 5. Measurement results of the PESC outcome along the coronal plan: A – boxplot of the vertical distances; B – boxplot of the horizontal distances; and, C – illustration of how the measurements were made (arrows representing the directions in which the distances were measured according to the greatest depression point, center in yellow).

The second group of measurement parameters performs a tridimensional analysis in each patient SCIA. Fig. 6A presents the average of the distances between the anterior chest wall meshes, acquired before and after the surgical correction, of different patients. The results show a mean distance depression of 12 mm (± 8.7 mm) in all patients. For high deformities this value could increase significantly, up to 35 mm. It was also measured the mean value of the greatest distance of the deformity (largest depression point) with value equal to 27.9 mm (± 9.1 mm). Fig. 6B shows how the SCIA changes along the coronal plan, where 75% of the patients present a SCIA between $21.5 \times 10^3 \text{ mm}^2$ and $27.5 \times 10^3 \text{ mm}^2$. Fig. 6C presents the results of the volume of the SCIA, between the two anterior chest wall meshes (acquired before and after PESC). The measurement of this parameter indicates that the mean volume is equal to $152 \times 10^3 \text{ mm}^3$ ($\pm 94,5 \times 10^3 \text{ mm}^3$).

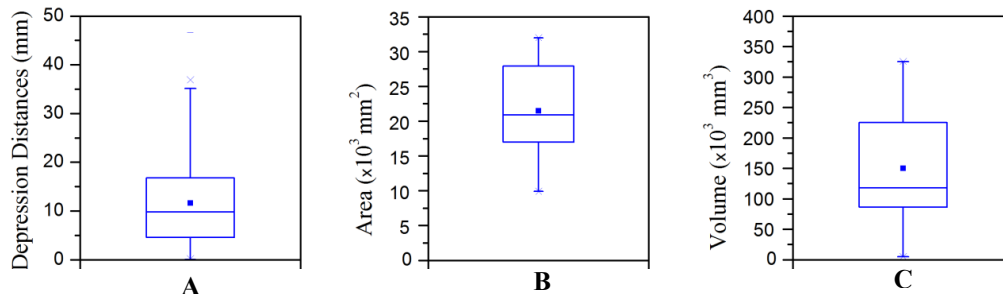


Figure 6. Tridimensional analysis of the SCIA.

3.5. Surface normalization

Ray-Triangle intersection is a computer graphics, method used in several scenarios, such in this work one analyses the possibility of the development of a software tool intersection method that is a variant of Möller-Trumbore algorithm with the advantage of not having pre-computed plane equations and reduced memory usage. This method measures the *pectus excavatum* deformity differences, before (red dots, Fig. 7) and after (green dots, Fig. 7) surgical correction, based on the distance between two triangle meshes resulting from the VOI selection (blue dots, Fig. 7): VOI of the anterior chest wall before PESC (red dots, Fig. 7) and VOI of the anterior chest wall after PESC (green dots, Fig. 7).

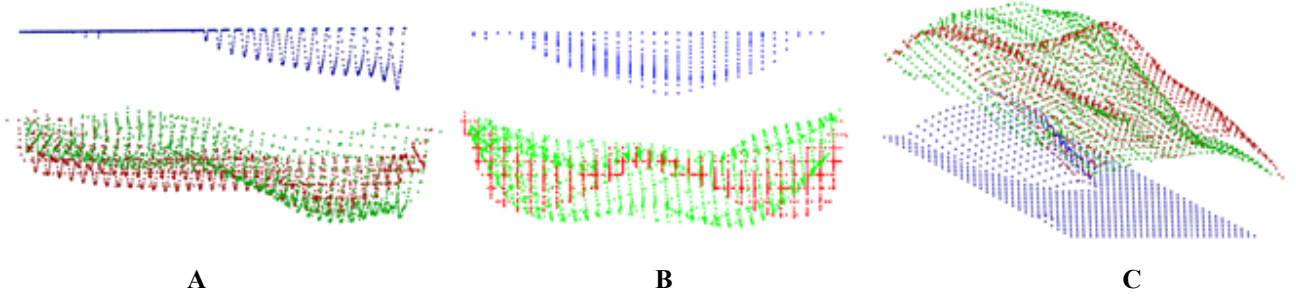


Figure 7. Sampling of two triangle meshes for measuring the deformity differences of *pectus excavatum*: a) sagittal view; b) axial view; c) perspective view. Green: VOI points of the anterior chest wall gathered after PESC; Red: VOI points of the anterior chest wall gathered before PESC; Blue: differences between the red and green points.

For all patients, a grid of 16x16 points equally spaced was used to sample the distances from the two triangle meshes. The grid size was adjusted for the dimension of each VOI. Therefore, for each grid point $Gp(i)$ (with $i = 0, 1, 2, \dots, N$, with N being the total number of grid points) it was defined a ray $R(i)$, normal to XZ plan, starting in $P(i)$ and ending at $Rtop(i)$ (point above the mesh). Then, it was checked if it intersects on one of the meshes $T(j)$ (with $j = 0, 1, 2, \dots, Nt$, with Nt being the total number of mesh triangles). For that, $T(j)$ was defined as a plan, allowing the calculation of its parametric equation and the computation of its parametric coordinates of the intersection point $P(i)$ to the ray. After the detection of two intersections for each grid point, one for each mesh, the difference between the two intersected points was calculated, and it was established the distances between the two meshes (blue dots, Fig. 7).

3.6. Artificial Neural Networks

This subsection describes the development of an ANN whose goal is to generate a function capable of predicting the outcome of PESC.

Two different networks topology were used, namely feed-forward neural networks (FNN) (Fig. 8A) and cascade-forward neural networks (CNN) (Fig. 8B), due to their ability to approximate non-linear functions.

FNN and CNN were developed with one and two hidden layers with sigmoid neurons, followed by an output layer of linear neurons (the network output can take any value), preceded by an input layer. The input and output layer sizes were determined from the input (normalized points of the anterior thoracic wall gathered before PESC: red dots, Fig. 7) and target (normalized points of the anterior thoracic wall gathered after PESC: blue dots, Fig. 7) vectors, respectively (256 points).

Neurons in the input layer had no activation function. The neurons in the hidden layer sum the weighted inputs and pass the resulting summations through a nonlinear activation function to the output neuron or adjacent neurons.

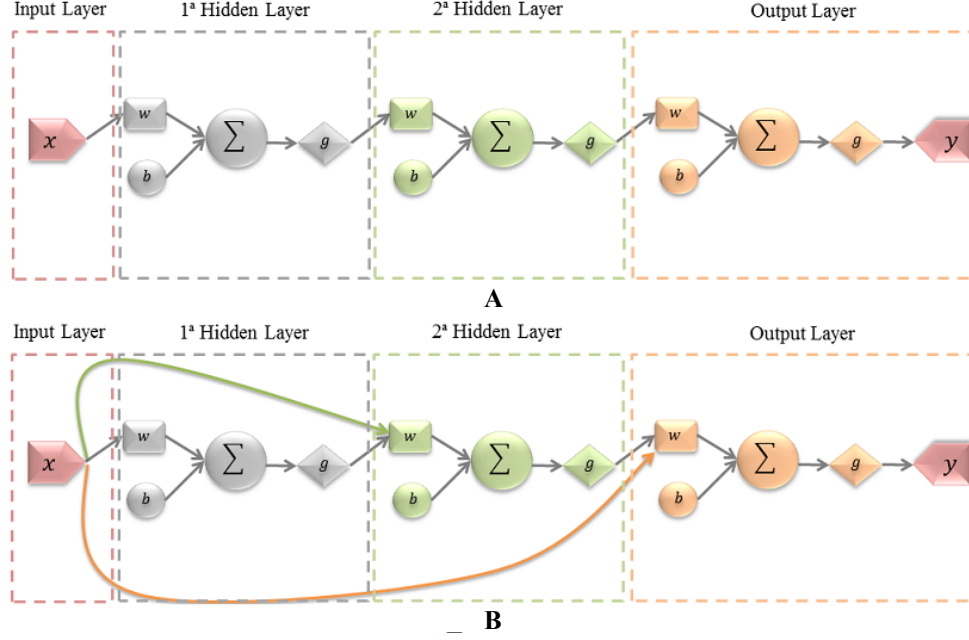


Figure 8. Illustration of a FNN topology (A) and a CNN topology (B) where: x is the input vector; g is the activation function for each layer; w is the weight of each input in each layer; and, y is the network output.

Once the network architecture was created, the network weights (w , Fig. 8) and biases (b , Fig. 8) were randomly initialized, leaving the network ready for training, based on the network inputs and targets.

During training, the weights and biases of the network were iteratively adjusted to minimize the network performance function. The performance function used, measures, the mean squared error (MSE) between the network outputs and the target outputs (Eq. 3), during a training procedure.

$$MSE = \frac{1}{N} \sum_{i=1}^N (V_o(i) - V_t(i))^2 \quad (3)$$

Where N is the total number of points used in the training vectors, V_o is the outputs vector of the ANN and V_t is the targets vector.

Four different training algorithms for FNN and CNN were used to determine the adjustment of weights and biases: Scaled Conjugate Gradient (SCG), Levenberg-Marquardt (LM), Resilient Back propagation (RP), and One Step Secant (OSS) [31-34]. These algorithms are based on the gradient of the performance function determined using a backpropagation technique. Within this technique the network weights and biases are moved along the negative gradient of the performance function.

When properly trained with input/targets relationships, backpropagation networks leads to reasonable outputs, even when presented with inputs that have never been provided to the network before.

ANN performance was evaluated through a statistical regression analysis method, which returns three parameters: m , b and R values. The first two correspond to the slope and O_y axis intersection of the best linear regression between the output and target vector, respectively. If the outputs are exactly equal to targets, m would be 1 and b would be 0. The R parameter is the correlation coefficient between the outputs and targets, and its value is as close to 1 as the outputs are best fitted with the targets.

4. RESULTS

Within the current project, neuronal networks were trained towards the goal of generating a function capable of estimating the postsurgical outcome of PESC. Since the quantity of female patients was reduced, all of the ANN developed were trained and tested with male patients.

All tests discussed in this section were especially directed to find the best training parameters. This is justified by the fact that there is no theoretical background concerning how different training algorithms will perform from such input/target vectors relationships. Consequently, the best ANN model was found by a repetitive trial-and-error process, during which, different training parameters and backpropagation algorithms were examined and compared.

Commonly, there are four elements that comprise the ANN architecture: the number of layers; the number of neurons in each layer; the activation function of each layer (g, Fig. 6); and the training algorithm.

The activation functions were chosen based on each layer. For instance, the identity function was used in the output layer, while a continuous nonlinear sigmoid function was used in the hidden layers.

Regarding the number of layers and neurons of each layer, in the beginning of the training procedure, four different ANN objects were created:

- A single layer FNN with 20 neurons in the hidden layer (FNN20);
- A single layer CNN with 20 neurons in the hidden layer (CNN20);
- A two-layer FNN with 20 neurons in each hidden layer (FNN20_20);
- A two-layer CNN with 20 neurons in each hidden layer (CNN20_20);

Afterwards, all models were trained with a randomly selected subset of 60% of the patients and 20% was used to validate the network generalization (the ability to identify and respond to cases that are similar but not identical to the ones that it has been trained with). The other 20% of patients were used to test the final network model with new inputs that the network had never experienced before.

The training procedure was implemented under Matlab [35], and it was repeated 15 times for each network object. Between each iteration, the network weights and biases were initialized in order to allow new solutions. In the end, the network object with minimal MSE was chosen to predict PESC outcome, while the other networks objects were discarded.

The training was performed according the followed configurations:

- Number of epochs during training: 1000;
- Maximum number of iterations in which the gradient error increases: 10;
- Minimum error gradient for which the training process ends: 1×10^{-8} .

The backpropagation technique with SCG, LM, OSS and RP learning algorithm were used to train CNN and FNN (results in Fig. 9 in black and blue, respectively). Each training algorithm has its own characteristics. LM and SCG algorithms were the fastest ones to obtain a solution.

The best results were obtained through the SCG algorithm, with R and m closest to 1 and b closest to 0, for both network architectures. In what concerns to R , m and b values, FNN presented smoother oscillations around the average value, allowing more accurate results than the ones obtained by CNN. The worst results occurred when CNN was used with the RP and OSS training algorithm for both network topologies.

The most critical elements during the training process of all ANN objects were the training algorithm and the number of hidden layers and hidden neurons. Unfortunately, it is not possible to theoretically determine how many hidden layers or neurons are needed for each problem and what are the best training algorithms.

The number of hidden layers and neurons were especially important, because they largely affect the generalization ability due to the overfitting of the training data. This may be a reason why a FNN20 performed better than a FNN2020 and a FNN20 performed better than a single hidden layer FNN with 40 neurons. Moreover, a high number of network neurons

slowed down the training process, whereas a reduced number decreases the network performance because the network is not able to learn the proposed problem (e.g. 10 neurons).

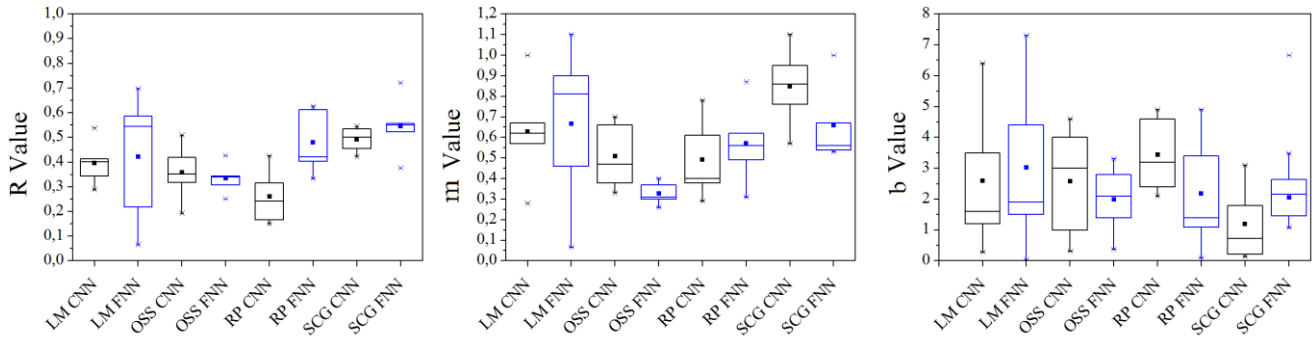


Figure 9. Boxplots of R , b and m values of the statistical regression of the ANN performance. In Ox axis each abbreviation represents the training algorithm and the network topology (e.g. LM CNN represents a cascade-forward network trained with Levenberg-Marquardt). The square represents the mean values for each study.

The number of neurons in each hidden layer was systematically modified to obtain a reliable mathematical model to fit the input/target relationships and to obtain a reduced MSE. The best combination on the number of neurons and hidden layers were achieved by adding, individually, neurons or hidden layers, when the training was slow or when the MSE was large. On the other hand, neurons or hidden layers were removed when an increase did not correspond to a change in the network response.

Fig. 10 illustrates a sample result of statistical regression (R value) of test data, for several neurons of a FNN trained according to the LM algorithm. It can be verified that 20 neurons is the amount that presents R values with mean value closer to 1. Such an amount of neurons proved to be the most adequate value to establish relations between input and targets with less processing time for all network objects and training algorithms.

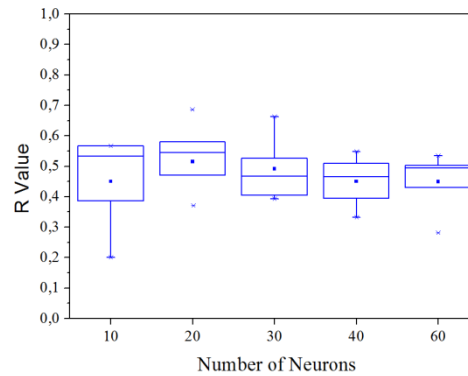


Figure 10. Boxplots of the R values of the statistical regression of the ANN performance when trained with several number of neurons and the SCG as training algorithm.

The results obtained with ANN showed that the agreements between the data acquired from the CT mesh before surgery and the data acquired using the 3D scanner after surgery are rare. Often, ANN did not converge to a solution producing a lower correlation coefficient between the outputs and targets (R value in the statistical regression analysis). Consequently, it proves that there are no relationships between all studied patients before and after surgical correction.

5. CONCLUSIONS

This paper presents a study – involving 21 male patients – of the evolution of the thoracic wall surface before and after *pectus excavatum* surgical correction (PESC). We have also analyzed, for the same group of patients, the degree of convergence of the thoracic wall surface.

The results were achieved through a methodology involving a combination of different computational techniques, such as image processing and computer graphics algorithms. These techniques allowed the affine registration between the anterior wall chest meshes, acquired before and after PESC. Subsequently, a series of 3D measures in both surfaces were made, permitting the definition of a SCIA, which was intended to be used for the simulation and prediction of *pectus excavatum* postoperative outcome.

Based on the obtained results, the difficulties in finding common characteristics in different patients were reinforced. In particular, the influence of physical characteristics was especially relevant, namely morphology deformity, degree of asymmetry, prosthesis shape and placing point, and patient age in postsurgical result.

Although this work aimed at the prediction of the surgical outcome of *pectus excavatum* correction, in this research one has discovered that for this particular problem, the technique employed – Artificial Neural Network (ANN) – rarely converges to a solution. Therefore, within this work it was not possible to obtain a satisfactory mathematical model with a desirable confidence level that could sustain the development of a software application.

Hereupon, new research paths based on this work have to be investigated. Furthermore, one expects that an increased number of patients to train, validate and test ANN, is one of the most promising paths to invest in. Another possibility to increase the results reliability would be to classify the patients into groups of various morphologic types of *pectus excavatum*, namely asymmetry defect of the thoracic wall; a defined, deep and localized concavity; and, a wider and shallower concavity.

ACKNOWLEDGMENTS

The authors of this work would like to thank the Department of pediatric surgery of Hospital de S. João of Porto. This work was supported by “Fundação para a Ciência e a Tecnologia”, Portugal (FCT) through the Postdoc grant referenced SFRH/BPD/46851/2008 and R&D project referenced PTDC/SAU-BEB/103368/2008.

REFERENCES

- [1] D. H. Kim, J. J. Hwang, M. K. Lee *et al.*, “Analysis of the Nuss procedure for pectus excavatum in different age groups,” *Annals of Thoracic Surgery*, 80(3), 1073-1077 (2005).
- [2] G. Krasopoulos, M. Dusmet, G. Ladas *et al.*, “Nuss procedure improves the quality of life in young male adults with pectus excavatum deformity,” *European Journal of Cardio-Thoracic Surgery*, 29(1), 1-5 (2006).
- [3] D. Nuss, R. E. Kelly, D. P. Croitoru *et al.*, “A 10-year review of a minimally invasive technique for the correction of pectus excavatum,” *Journal of pediatric surgery*, 33(4), 545-552 (1998).
- [4] D. N. Nuss, VA), Beuse, Francois (Callahan, FL), Stone, Kevin T. (Jacksonville, FL), Croitoru, Daniel (Norfolk, VA), Gordon, Jeffrey David (Orange Park, FL), Duncan, Jeffrey A. (Jacksonville, FL), Schumacher, Brian S. (Jacksonville, FL), [Method and apparatus for performing pectus excavatum repair] Walter Lorenz Surgical, Inc. (Jacksonville, FL), United States (2000).
- [5] D. Nuss, D. P. Croitoru, R. E. Kelly *et al.*, “Review and discussion of the complications of minimally invasive pectus excavatum repair,” *European Journal of Pediatric Surgery*, 12(4), 230-234 (2002).
- [6] M. L. Lawson, R. B. Mellins, M. Tabangin *et al.*, “Impact of pectus excavatum on pulmonary function before and after repair with the Nuss procedure,” *Journal of pediatric surgery*, 40(1), 174-180 (2005).
- [7] L. Molins, J. J. Fibla, J. Perez *et al.*, “Chest wall surgery: Nuss technique for repair of pectus excavatum in adults,” *MMCTS*, 2007(0102), 315- (2007).
- [8] A. Yardimci, “Soft computing in medicine,” *Applied Soft Computing*, 9(3), 1029-1043 (2009).

- [9] P. J. Lisboa, and A. F. G. Taktak, "The use of artificial neural networks in decision support in cancer: A systematic review," *Neural Networks*, 19(4), 408-415 (2006).
- [10] C. Archambeau, J. Delbeke, C. Veraart *et al.*, "Prediction of visual perceptions with artificial neural networks in a visual prosthesis for the blind," *Artificial Intelligence in Medicine*, 32(3), 183-194 (2004).
- [11] M. Ohlsson, "WeAidU - a decision support system for myocardial perfusion images using artificial neural networks," *Artificial Intelligence in Medicine*, 30(1), 49-60 (2004).
- [12] M. Ceylan, R. Ceylan, Y. Ozbay *et al.*, "Application of complex discrete wavelet transform in classification of Doppler signals using complex-valued artificial neural network," *Artificial Intelligence in Medicine*, 44(1), 65-76 (2008).
- [13] W. G. Baxt, "Application of Artificial Neural Networks to Clinical Medicine," *Lancet*, 346(8983), 1135-1138 (1995).
- [14] R. Ceylan, Y. Ozbay, and B. Karlik, "A novel approach for classification of ECG arrhythmias: Type-2 fuzzy clustering neural network," *Expert Systems with Applications*, 36(3), 6721-6726 (2009).
- [15] M. Egmont-Petersen, D. de Ridder, and H. Handels, "Image processing with neural networks - a review," *Pattern Recognition*, 35(10), 2279-2301 (2002).
- [16] H. A. Abbass, "An evolutionary artificial neural networks approach for breast cancer diagnosis," *Artificial Intelligence in Medicine*, 25(3), 265-281 (2002).
- [17] P. G. Benardos, and G. C. Vosniakos, "Optimizing feedforward artificial neural network architecture," *Engineering Applications of Artificial Intelligence*, 20(3), 365-382 (2007).
- [18] B. K. Lavine, and T. R. Blank, [Feed-Forward Neural Networks] Elsevier, Oxford(2009).
- [19] R. Teschl, W. L. Randeu, and F. Teschl, "Improving weather radar estimates of rainfall using feed-forward neural networks," *Neural Networks*, 20(4), 519-527 (2007).
- [20] Polhemus, [FastSCAN].
- [21] T. S. Yoo, "Insight into Images - Principles and Practice for Segmentation Registration, and Image Analysis," National Library of Medicine, NIH Office of high performance computing and Communications, 103-109.
- [22] J. C. Carr, R. K. Beatson, J. B. Cherrie *et al.*, [Reconstruction and representation of 3D objects with radial basis functions] ACM, (2001).
- [23] H. Huang, D. Li, H. Zhang *et al.*, [Consolidation of unorganized point clouds for surface reconstruction] ACM, Yokohama, Japan(2009).
- [24] M. Kazhdan, M. Bolitho, and H. Hoppe, [Poisson surface reconstruction] Eurographics Association, Cagliari, Sardinia, Italy(2006).
- [25] J.-D. Boissonnat, "Geometric structures for three-dimensional shape representation," *ACM Trans. Graph.*, 3(4), 266-286 (1984).
- [26] M. Soucy, and D. Laurendeau, "A General Surface Approach to the Integration of a Set of Range Views," *IEEE Trans. Pattern Anal. Mach. Intell.*, 17(4), 344-358 (1995).
- [27] V. V. Savchenko, A. A. Pasko, O. G. Okunev *et al.*, "Function Representation of Solids Reconstructed from Scattered Surface Points and Contours," *Computer Graphics Forum*, 14(4), 181-188 (1995).
- [28] J. C. Carr, R. K. Beatson, B. C. McCallum *et al.*, [Smooth surface reconstruction from noisy range data] ACM, Melbourne, Australia(2003).
- [29] G. Turk, and M. Levoy, [Zippered polygon meshes from range images] ACM, (1994).
- [30] D. Aiger, N. J. Mitra, and D. Cohen-Or, "4-points congruent sets for robust pairwise surface registration," *Acm Transactions on Graphics*, 27(3), - (2008).
- [31] M. F. Møller, "A scaled conjugate gradient algorithm for fast supervised learning," *Neural Networks*, 6(4), 525-533 (1993).
- [32] M. T. Hagan, and M. B. Menhaj, "Training Feedforward Networks with the Marquardt Algorithm," *Ieee Transactions on Neural Networks*, 5(6), 989-993 (1994).
- [33] Riedmiller, "Proceedings - IEEE International Conference on Neural Networks (ICNN)." 586-591.
- [34] R. Battiti, "First- and Second-Order Methods for Learning: Between Steepest Descent and Newton's Method," *Neural Computation*, 4(2), 141-166 (1992).
- [35] H. Demuth, M. Beale, and M. Hagan, [Neural Network Toolbox™ 6].